NANO LETTERS
Cite This: Nano Lett. XXXX, XXX, XXX−XXX
Letter
pubs.acs.org/NanoLett

A Reconfigurable Remotely Epitaxial VO_2 Electrical Heterostructure

Yuwei Guo,[†,○] Xin Sun,[‡,○] Jie Jiang,[†,§] Baiwei Wang,[†] Xinchun Chen,[∥,*] Xuan Yin,[∥] Wei Qi,[∥] Lei Gao,[⊥,*] Lifu Zhang,[†] Zonghuan Lu,[‡] Ru Jia,[†] Saloni Pendse,[†] Yang Hu,[†,‡] Zhizhong Chen,[†] Esther Wertz,[‡] Daniel Gall,[†] Jing Feng,[§] Toh-Ming Lu,[‡] and Jian Shi[†,#,*]

[†]Department of Materials Science and Engineering, Rensselaer Polytechnic Institute, Troy, New York 12180, United States
[‡]Department of Physics, Applied Physics, and Astronomy, Rensselaer Polytechnic Institute, Troy, New York 12180, United States
[§]Faculty of Material Science and Engineering, Kunming University of Science and Technology, Kunming 650093, China
[∥]State Key Laboratory of Tribology, Tsinghua University, Beijing 100084, China
[⊥]Beijing Advanced Innovation Center for Materials Genome Engineering, Institute for Advanced Materials and Technology, University of Science and Technology Beijing, Beijing, 100083, China
[#]Center for Materials, Devices, and Integrated Systems, Rensselaer Polytechnic Institute, Troy, New York 12180, United States

Supporting Information

ABSTRACT: The reconfigurability of the electrical heterostructure featured with external variables, such as temperature, voltage, and strain, enabled electronic/optical phase transition in functional layers has great potential for future photonics, computing, and adaptive circuits. VO_2 has been regarded as an archetypal phase transition building block with superior metal−insulator transition characteristics. However, the reconfigurable VO_2-based heterostructure and the associated devices are rare due to the fundamental challenge in integrating high-quality VO_2 in technologically important substrates. In this report, for the first time, we show the remote epitaxy of VO_2 and the demonstration of a vertical diode device in a graphene/epitaxial VO_2/single-crystalline BN/graphite structure with VO_2 as a reconfigurable phase-change material and hexagonal boron nitride (h-BN) as an insulating layer. By diffraction and electrical transport studies, we show that the remote epitaxial VO_2 films exhibit higher structural and electrical quality than direct epitaxial ones. By high-resolution transmission electron microscopy and Cs-corrected scanning transmission electron microscopy, we show that a graphene buffered substrate leads to a less strained VO_2 film than the bare substrate. In the reconfigurable diode, we find that the Fermi level change and spectral weight shift along with the metal−insulator transition of VO_2 could modify the transport characteristics. The work suggests the feasibility of developing a single-crystalline VO_2-based reconfigurable heterostructure with arbitrary substrates and sheds light on designing novel adaptive photonics and electrical devices and circuits.

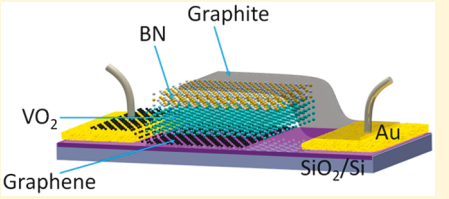

KEYWORDS: *Remote epitaxy, metal−insulator transition, heterostructure, diode*

Vanadium dioxide (VO_2) is a well-studied strongly correlated material due to its technological interests such as close to room-temperature metal−insulator transition (MIT) temperature for ultrafast Mottronics, infrared sensor, optical switches, field-effect switches, and nonlinear circuit components,[1−12] as well as rich physics stemming from the complex coupling among charge, spin, and lattice degrees of freedom. However, epitaxial or single-crystalline VO_2-based heterostructure devices are generally unavailable[13] due to both its chemical/electronic vulnerability in the growth of subsequent epilayers and its strict requirements on substrate lattice match. It is believed that having a free-standing single-crystal VO_2 could bring us much more design space in heterostructure devices since one can transfer such crystal to any substrate. Free-standing VO_2 film[14,15] receives far less study despite that heterostructures developed by free-standing films (e.g., Ge, Si, GaAs)[16] with mechanical transfer could be much superior to epitaxial films in terms of device performance since they do not need to relax the misfit strain by introducing dislocations.

Many phase-change heterostructures reported in literature are based on two-dimensional chalcogenide materials as a phase-change switchable interlayer due to their easy transfer and stacking according to device design.[17−19] Heterostructures based on crystalline three-dimensional materials such as VO_2 and $La_{1-x}Sr_xMnO_3$ highly rely on lattice-matched substrates and are not free-standing,[20−26] limiting their adaptability to a wider range of applications.

In this work, we develop the first remotely epitaxial VO_2 heterostructure, which allows us to make the phase-change VO_2/boron nitride heterostructure with tunable transport characteristics.[27−30] We grow high-quality VO_2 film on c-plane sapphire with graphene as an interface layer. It shows that the

Received: July 2, 2019
Revised: November 26, 2019
Published: November 26, 2019

DOI: 10.1021/acs.nanolett.9b02696
Nano Lett. XXXX, XXX, XXX−XXX

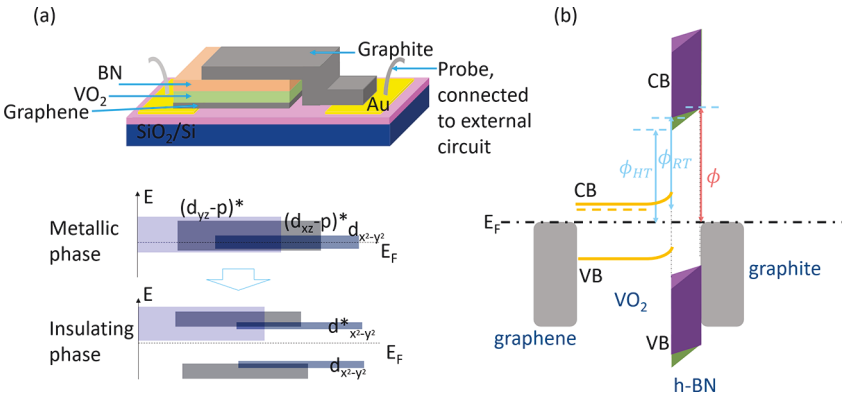

Figure 1. Design principle. (a) Structure model of the vertical diode device (top). Upon MIT, a shift of spectral weight leads to a change of energy band (bottom). (b) Band structure of the vertical diode device. The purple bands of h-BN stand for bands tilting when VO_2 is at the insulating phase, and ϕ_{RT} is the energy barrier at room temperature. The conduction band (CB) and valence band (VB) are also shown for insulating phase VO_2. The green bands of h-BN stand for bands tilting when VO_2 is at the metallic phase, and ϕ_{HT} is the energy barrier at high temperature. ϕ represents the energy barrier between the top graphite electrode and h-BN.

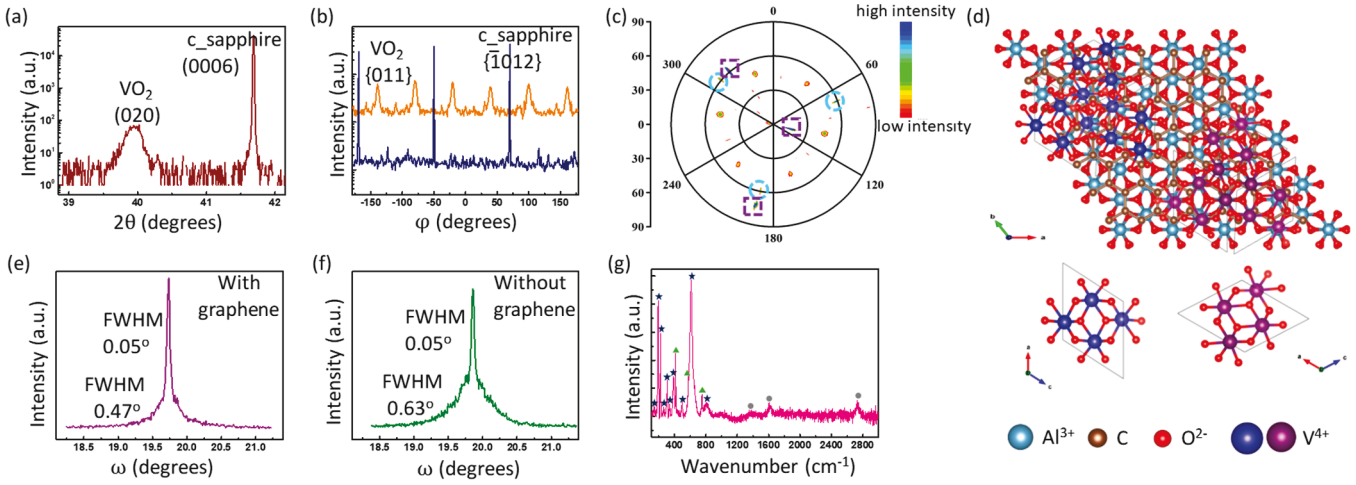

Figure 2. Structural analysis of remote epitaxial films. (a–c) XRD characterizations on VO_2 film grown on c-plane sapphire with graphene as an interface layer. (a) ω-2θ scan around the VO_2 (020) peak; (b) φ-scan of the VO_2 {011} peaks and c-plane sapphire $\{\bar{1}012\}$ peaks. (c) Pole figure: the six concentric dots represent VO_2 {011} peaks, and the three dots selected by cyan color circles are from c-plane sapphire $\{\bar{1}012\}$ peaks. Three spots selected by purple squares correspond to noises. (d) Atomic model displaying the two possible epitaxial relations between VO_2 and the c-plane sapphire substrate. The crystal axis on the upper left is for c-plane sapphire. In each possibility, there are three in-plane orientations of VO_2, 120° apart, on c-plane sapphire. The bottom two figures are VO_2 unit cells with an in-plane rotation of 60°. The axis orientations are also shown next to the unit cells. (e) Rocking curve on the VO_2 (020) peak for VO_2 film grown on c-plane sapphire with graphene as an interface layer. (f) Rocking curve on VO_2 (020) peak for VO_2 film grown on c-plane sapphire without graphene as an interface layer. (g) Raman spectrum of as-grown VO_2 film on a graphene transferred c-plane sapphire substrate. Blue stars indicate VO_2 peaks, green triangles indicate c-plane sapphire substrate peaks, and gray spheres indicate graphene peaks. XRD data are collected after samples experience 2 h of cooling in the PLD chamber at the oxygen pressure the same as their growth pressure.

insertion of a graphene layer between VO_2 and c-plane sapphire does not change the epitaxy relation in the case of direct epitaxy. Via mechanical transfer, we demonstrate a vertical diode device made from free-standing VO_2 that serves to show how the band structure change of VO_2 upon its MIT can tune the diode characteristics and achieve rectification behavior.

Phase-Change Heterostructure. The reconfigurable vertical device structure and fabrication process are shown in the top panel of Figure 1a. Hexagonal boron nitride (h-BN) is used as an insulating barrier layer between VO_2 and graphite. The free-standing VO_2 is grown on graphene via pulsed laser deposition (PLD). Both top graphite and bottom graphene electrodes are connected to gold electrode pads deposited on the SiO_2 substrate. It is designed (as shown in the bottom panel of Figure 1a) that VO_2 serves as the reconfigurable part due to its MIT transition resulting in a spectral weight and Fermi level shift.[31] The transition brings a tunable barrier height in the VO_2/BN interface (Figure 1b). In the VO_2/BN/graphite heterostructure, the dissimilar contacts of BN and the corresponding barrier heights (φ_{HT}, φ_{RT}, and φ illustrated in Figure 1b) (either metal VO_2 and graphite or insulator VO_2 and graphite) would bring asymmetric transport characteristics. Upon MIT, the change of barrier height at the VO_2 side (e.g., from φ_{HT} to φ_{RT}) would modify the asymmetric transport characteristics. This heterostructure not only demonstrates its application as a temperature-controlled switch but also may reveal some structures and devices that can be made from free-standing VO_2 films.

DOI: 10.1021/acs.nanolett.9b02696
Nano Lett. XXXX, XXX, XXX−XXX

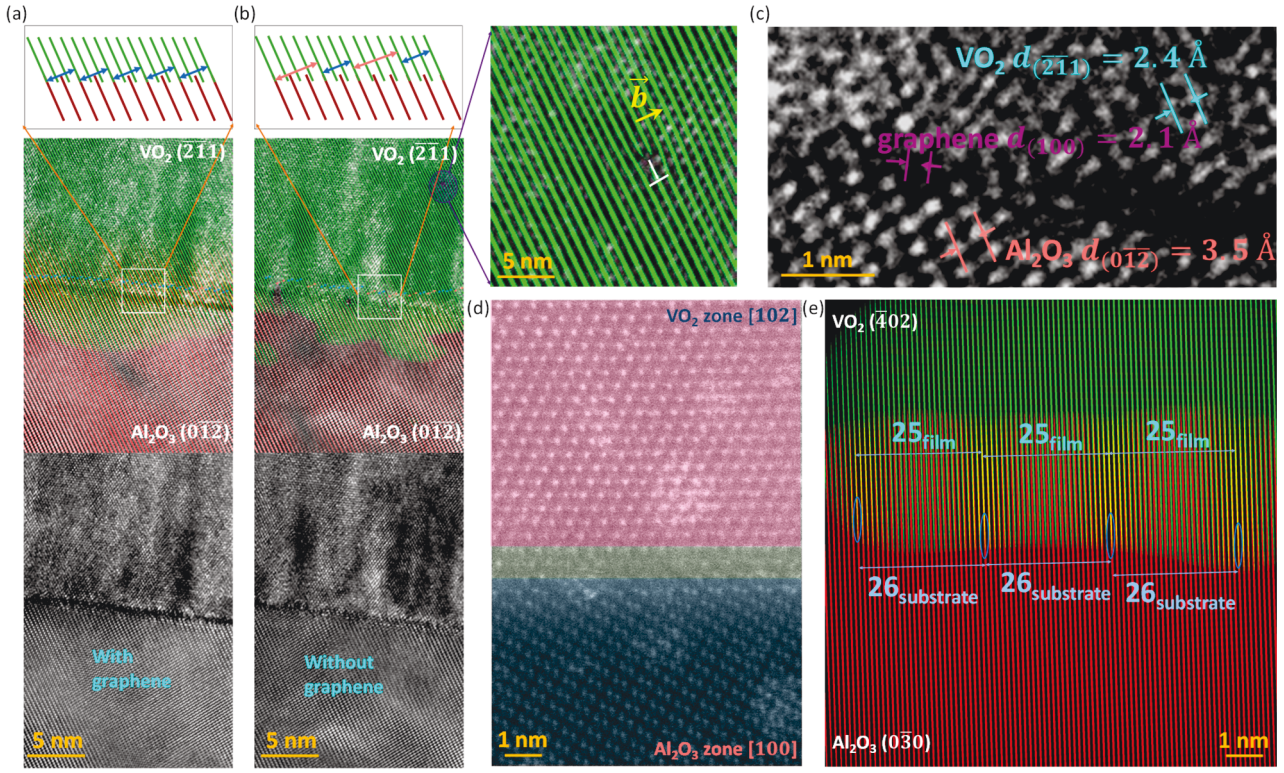

Figure 3. Microscopy characterization of epitaxy relation and dislocations. (a, b) HRTEM images (bottom) and their images overlapped with inverse FFT lattice fringes (middle) for VO_2 $(\bar{2}\,\bar{1}\,1)$ and Al_2O_3 $(0\,\bar{1}\,\bar{2})$ with (a) and without (b) graphene at the local interface region. The enlarged lattice arrangement between film and substrate is illustrated by lines on the top panels. Inset of panel b: a dislocation is found in VO_2 film directly grown on c-sapphire. (c) HRTEM image zoomed in at the interface; *d*-spacings of VO_2 $(\bar{2}11)$, Al_2O_3 $(01\bar{2})$, and graphene (100) are shown. (d) Cs-corrected STEM image of VO_2-graphene-c-plane sapphire. The pink, green, and dark blue colors highlight regions of film, interface, and substrate, respectively. (e) Fringes generated from inverse FFT of STEM images (d) of VO_2 $(\bar{4}02)$ and Al_2O_3 $(0\bar{3}0)$ are shown in green and red, respectively. It is seen that the 26 *d*-spacing of Al_2O_3 $(0\bar{3}0)$ matches the 25 *d*-spacing of VO_2 $(\bar{4}02)$.

Remote Epitaxy of VO_2 Film. PLD technic is used to grow free-standing VO_2 on a c-plane sapphire substrate with transferred graphene as an interface layer, followed by annealing (see supplementary methods for details). The thickness of the VO_2 film is about 100 nm, as shown in the cross-sectional SEM images in Figure S1. The morphology of the film before and after annealing is also studied under SEM, as shown in Figure S2. The surface became smoother after annealing.

The structure of VO_2 film is characterized by X-ray diffraction with either the whole film grown on graphene or without graphene (see supplementary methods for details). The ω-2θ scan is conducted using a parallel-beam configuration with an X-ray hybrid mirror around the VO_2 (020) peak, as shown in Figure 2a. The X-ray hybrid mirror helps to get rid of Cu Kα_2 signals and generate well-defined peaks at the expense of peak intensity. The ω-2θ scan with an X-ray mirror is also shown in Figure S3a. The out-of-plane direction is the normal direction of the plane (020) for VO_2 and (0006) for a c-plane sapphire. Even though the interplanar spacing of (020) and (002) planes of VO_2 are very close, we determine that the out-of-plane direction for VO_2 is actually the normal of the (020) plane by conducting a φ-scan of VO_2 {011} planes. If assuming the out-of-plane direction of the VO_2 film is plane normal of (002), and setting the κ angle corresponding to {011} planes, no peak shows up in the φ-scan (Figure S3b). However, if we choose the out-of-plane direction as the plane normal of (020), six peaks show up in the φ-scan with intervals of 60° (Figure 2b). Since the monoclinic VO_2 (011) peak has a multiplicity of two, this indicates that there are three types of in-plane orientations of VO_2 film, and they are 120° away from each other.

This is further characterized by the pole figure for VO_2 {011} in Figure 2c. The orientations between VO_2 and c-plane sapphire are shown in the atomic model in Figure 2d. There are two possibilities, shown in blue and purple of the VO_2 structure, for the arrangement of three in-plane orientations of VO_2 on c-plane sapphire with graphene. The epitaxial relation is c-plane sapphire (0006) ‖ VO_2 (020) and c-plane sapphire $[1\bar{1}00]$ ‖ VO_2 [001] (blue VO_2 atomic structure), or c-plane sapphire $[1\bar{1}00]$ ‖ VO_2 $[\bar{1}00]$ (purple VO_2 atomic structure). The pole figure on bare c-plane sapphire with the same measurement conditions is shown in Figure 3b. It shows three spots contributed by $\{\bar{1}012\}$ with 3-fold symmetry, and other signals are noises from the system. Our experimental results show that the graphene layer on c-plane sapphire does not change the epitaxial relation found in direct epitaxy between VO_2 film and c-plane sapphire. Based on the epitaxial relation, there are +2.0% tensile and −4.7% compressive misfit along the monoclinic VO_2 [001] and [100] direction with respect to bare c-plane sapphire, respectively. It is worth noting that the VO_2 film grown on c-plane sapphire with the graphene interface layer has better crystallinity compared to the film grown on bare c-plane sapphire, as shown in their rocking curves of (020) in Figure 2e,f. The sharper high-intensity peak with fwhm of 0.05° for both samples is attributed to the

DOI: 10.1021/acs.nanolett.9b02696
Nano Lett. XXXX, XXX, XXX−XXX

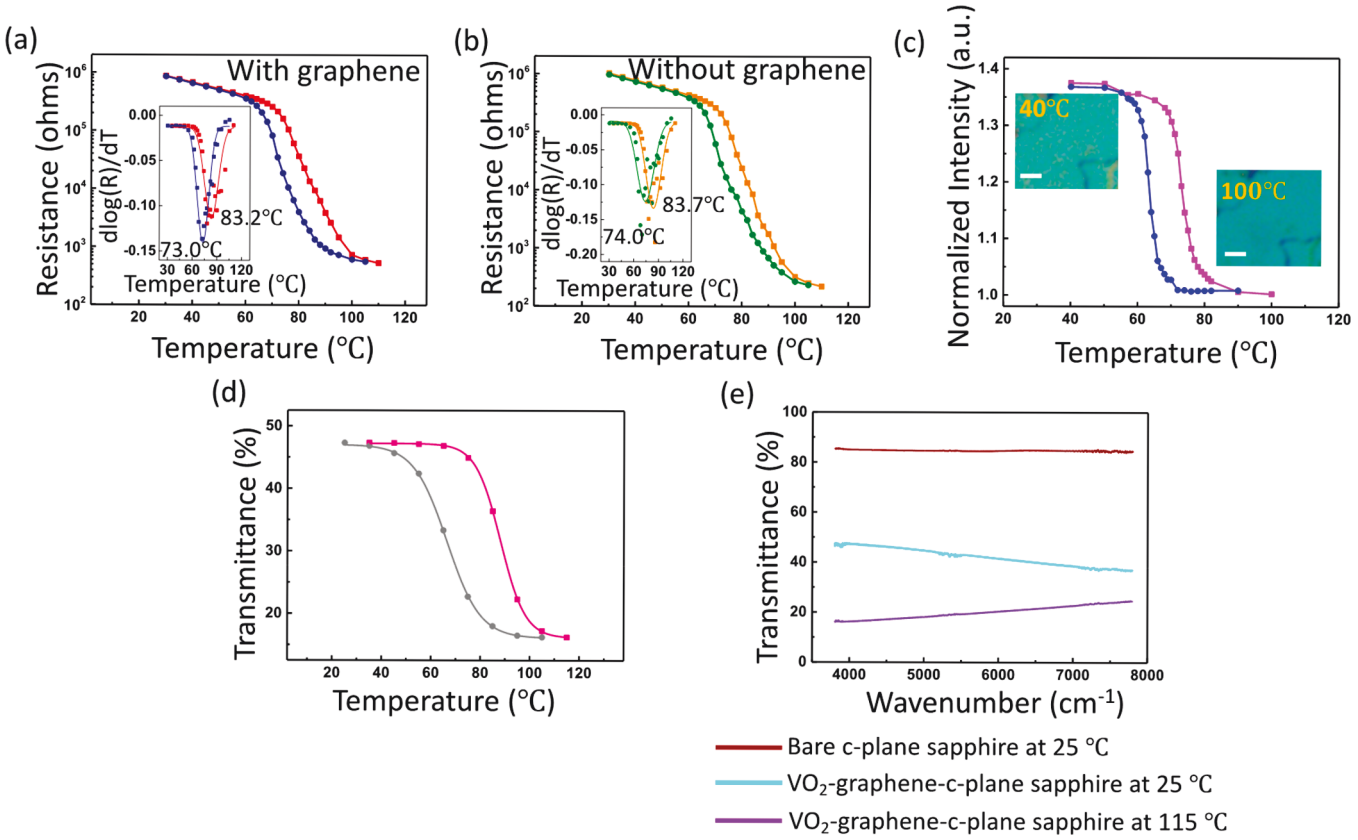

Figure 4. Electrical and optical properties. (a, b) Resistance vs temperature curve for VO_2 grown on c-plane sapphire with or without a graphene interface layer, respectively. The inset is the corresponding d[log(resistance)]/d[temperature] curves. (c) Optical intensity contrast of the VO_2 film on graphene (transferred onto the SiO_2 substrate) varies with temperature. The average intensity of VO_2 is normalized by the background intensity from SiO_2. The inset figures are optical images of the sample at 40 °C (insulating phase) and 100 °C (metallic phase). The scale bar for the image is 5 μm. (d) Temperature-dependent transmittance at 4000 cm^{-1} (~0.50 eV) of VO_2 grown on c-plane sapphire with graphene. (e) Transmittance of VO_2 grown on c-plane sapphire with graphene and bare c-plane sapphire measured from 3800 to 7800 cm^{-1}.

strained interface layer, while the broader low-intensity peak corresponds to the strain-relaxed top layer. The VO_2 film grown on graphene has a narrower rocking curve for the strain-relaxed layer and, thus, higher crystal quality. The insertion of the graphene layer between VO_2 film and c-plane sapphire serves to reduce their epitaxial strain, so fewer defects such as dislocations are formed to relax such strain, leading to a better crystallinity.

Reduction in strain between the VO_2 film and substrate with a graphene interface layer is also confirmed by another ω-2θ scan on VO_2 films grown on c-plane sapphire with and without graphene at a higher oxygen pressure (10 mTorr) in PLD (Figure S3d). Both 2θ shift to smaller values due to reduced oxygen vacancies.[32,33] VO_2 film grown on bare c-plane sapphire has a larger 2θ value, indicating a smaller (020) interplanar distance, and thus larger compression strain in the out-of-plane direction.

It is known that graphene damage is common in PLD due to oxygen plasma,[34,35] although it can remain stable below 500 °C in air.[36] However, for the quality of graphene after PLD growth, we checked local regions by Raman spectra. Strong characteristic Raman peaks from graphene and VO_2 were observed, while the graphene D band remained at a low intensity both after growth and after being exfoliated and transferred onto the SiO_2 substrate (Figure 2g, Figure S4). Besides, the fact that VO_2 film can be peeled off from the c-plane substrate and shows good performance in the device suggests that, in some regions of the substrate, graphene is still functioning though there may be some damage. Nonetheless, the graphene layer may no longer be continuous after PLD, as discussed later.

Characterization of the rocking curve on exfoliated VO_2-graphene membranes was hindered by the low yield (<5%) of these membranes, each with a typical size of 10−30 μm. Instead, we obtained a rocking curve on the VO_2-graphene-c-plane sapphire sample after being peeled off three times. The sapphire substrate was originally fully covered by graphene and VO_2. The residue of VO_2-graphene on c-plane sapphire, which also experiences the energetic peeling off process, gives a stronger signal for rocking curve measurement, as shown in Figure S5. The fwhm is increased to 0.74°. However, the fact that the exfoliated VO_2-graphene membranes showed a strong VO_2 Raman signal (Figure S4) indicates that the phase of VO_2 is preserved.

To further characterize the graphene effect on epitaxial relation between VO_2 film and c-plane sapphire substrate, cross-sectional TEM and STEM images were obtained. The lower strain of VO_2 film was observed for film grown on graphene than that on bare c-plane sapphire (Figure 3). HRTEM images are shown at the bottom of Figure 3a,b. Inverse FFT lattice fringes (middle of Figure 3a,b) from the monoclinic VO_2 $(\bar{2}11)$ and Al_2O_3 $(0\bar{1}2)$ spots are shown in green and red lines, respectively. The FFT fringes are overlapped with the original TEM images for easier location

DOI: 10.1021/acs.nanolett.9b02696
Nano Lett. XXXX, XXX, XXX−XXX

of the interface. In Figure 3a, the majority of the area at the interface has graphene, while, in Figure 3b, there is an absence of graphene, as indicated in the image. Assuming VO_2 film is fully relaxed, we can calculate that the number of VO_2 fringes that matches the number of Al_2O_3 fringes is about 1.43 (see supplementary note 1 for details). At the presence of graphene, we can see that three VO_2 *d*-spacings match two Al_2O_3 *d*-spacings (the number of film and substrate fringes ratio is 1.5), while, without graphene at the interface, four VO_2 *d*-spacings match three Al_2O_3 *d*-spacings (the number of film and substrate fringes ratio is 1.33). As we can see from these ratios, VO_2 film grown on graphene has a *d*-spacing close to its bulk value (since $|1.43-1.33| > |1.5-1.43|$). This is as expected since the graphene insertion layer reduces the interaction between the sapphire substrate and film. Besides, we do not see dislocations in VO_2 film grown on graphene. For film grown on bare c-plane sapphire, we see dislocation, and also the above ratio of numbers of *d*-spacings of film and substrate decreases. A smaller ratio means that VO_2 *d*-spacing is larger than its bulk value, suggesting that it is under tensile strain from the substrate.

Figure 3c shows a TEM image zoomed in at the interface to demonstrate the existence of a possible graphene layer. The atom spacing at the interface matches the (100) *d*-spacing of graphene. Figure 3d shows a Cs-corrected STEM image at a larger area, and different colors represent the film, substrate, and interface, respectively. We select FFT spots of VO_2 $(\bar{4}02)$ and Al_2O_3 $(0\bar{3}0)$ from Figure 3d and generate their corresponding fringes in the image in Figure 3e. The blue circles highlight locations where fringes of VO_2 film and c-plane sapphire substrate match best. We found that 25 VO_2 $(\bar{4}02)$ *d*-spacings match 26 Al_2O_3 $(0\bar{3}0)$ *d*-spacings, representing an almost relaxed lattice spacing of the film (see supplementary note 1 for details). Besides, there are also no dislocations observed in the VO_2 film.

In summary, our cross-sectional TEM and Cs-corrected STEM images confirm that the presence of graphene at the interface can reduce the misfit strain between substrate and film, so fewer dislocations are required to release the strain. Thus, higher crystallinity is expected in VO_2 film grown on c-plane sapphire with the graphene insertion layer.

Metal–Insulator Transition of Remote Epitaxial Films. After confirming that we obtain good crystallinity of epitaxial VO_2 on c-plane sapphire with and without graphene, we further characterize their metal–insulator transition (MIT) by measuring resistance vs temperature ($R-T$) curves (Figure 4a,b) (see supplementary methods for details). To rule out other impacts, we always keep the two devices/samples from the same c-plane sapphire half covered by graphene and the other half without graphene. VO_2 film grown on c-plane sapphire either with or without the graphene interface layer shows reasonable resistance change across the MIT, defined by a ratio of electrical resistance at 30 and 110 °C, of 1.6×10^3 and 4.6×10^3, respectively. The reasonable resistance change indicates limited midgap states in the semiconductor VO_2, which would otherwise reduce its resistance.

We note that VO_2 grown on graphene has a lower transition temperature during both increasing and decreasing temperature processes. This can be explained by a smaller in-plane tensile strain due to the presence of a graphene layer.[37,38] The in-plane tensile strain increases the phase transition barrier by an increasing distance between vanadium ions,[37,39,40] so the film grown on the c-plane sapphire with a graphene interface layer has a 0.5–1° lower transition temperature compared to that grown on bare c-plane sapphire.

The thermal hysteresis, ΔH, defined as the difference between transition temperature in heating and cooling cycles,[37] is 10.2 and 9.7 °C for VO_2 film grown on graphene and bare c-plane sapphire, respectively. ΔH is directly related to ΔT, the temperature difference between experimental temperature T and the equilibrium phase transition temperature.[37,41] VO_2 film grown on graphene has a larger ΔT, so it has a slower phase transition rate. The total change in free energy during phase transition in a defect-free crystal is $\Delta G_r = -\frac{4}{3}\pi r^3 \Delta G_V + 4\pi r^2 \gamma$ (assuming a homogeneous spherical model and the argument applies for a heterogeneous nucleation), where r is the radius of the nucleus, ΔG_V is the difference in free energy per unit volume of the metallic and insulating phases at experimental temperature T, and γ is the interfacial free energy per unit area between the metallic and insulating phases. The nucleation energy barrier ($\Delta G^* = \frac{16\pi\gamma^3}{3(\Delta G_V + \Delta G_D)^2}$, where ΔG_D is the free energy per unit volume increase due to the presence of defects in a defective crystal[42]) determines the nucleation rate in an exponential manner. Larger hysteresis indicates a lower nucleation rate and thus a higher energy barrier. According to the transport results, the remote epitaxial film sees a large energy barrier, which is reasonable since it has fewer defects that reduce the denominator term in the energy barrier.

We would also like to point out that, at the metallic phase, VO_2 grown on c-plane sapphire without graphene shows a smaller resistance, probably due to thicker VO_2 film grown on bare c-plane sapphire. Even though with the same experimental condition, the wetting between VO_2 and c-plane sapphire without graphene is better, leading to higher nucleation and growth rates. The sharpness of the transition is characterized by the fwhm of the $d\log(R)/dT$ vs temperature curve, which is not affected by the transition amplitude.[10,43–46] As shown in the inset of Figure 4a,b, it is 19.9 and 16.8 °C for VO_2/graphene/c-plane sapphire during the increasing and decreasing temperature region, respectively, compared to 21.6 and 24.0 °C for the film without a graphene interlayer, respectively. The sharper phase transition confirms the low defect density and high crystallinity of VO_2 film grown on graphene, agreeing with its narrower rocking curve observed for the remote epitaxial film. This idea is on the contrary to the effort in employing lattice strain to grow epitaxial film or tune film properties. However, the release of epitaxial strain indeed improves film crystal quality, and the choice of graphene as an intermediate template not only preserves the epitaxy relation between film and substrate but also realizes the achievement of free-standing VO_2 by releasing the graphene layer from the substrate after film deposition.

Besides characterizing the resistance change across MIT, it is also interesting to capture the dynamic process on how the metallic domains appear and expand as the temperature increases above the MIT temperature. An intensity contrast observed under an optical microscope of insulating and metallic domains is well reported for single-crystal VO_2 nanobeams.[47–49] Unfortunately, less work is devoted to characterizing the insulating and metallic domains revolution in free-standing VO_2 thin films.[50] Here, we observe a change in optical contrast with the temperature of VO_2 film on graphene after dry transfer from the c-plane sapphire substrate onto the

DOI: 10.1021/acs.nanolett.9b02696
Nano Lett. XXXX, XXX, XXX–XXX

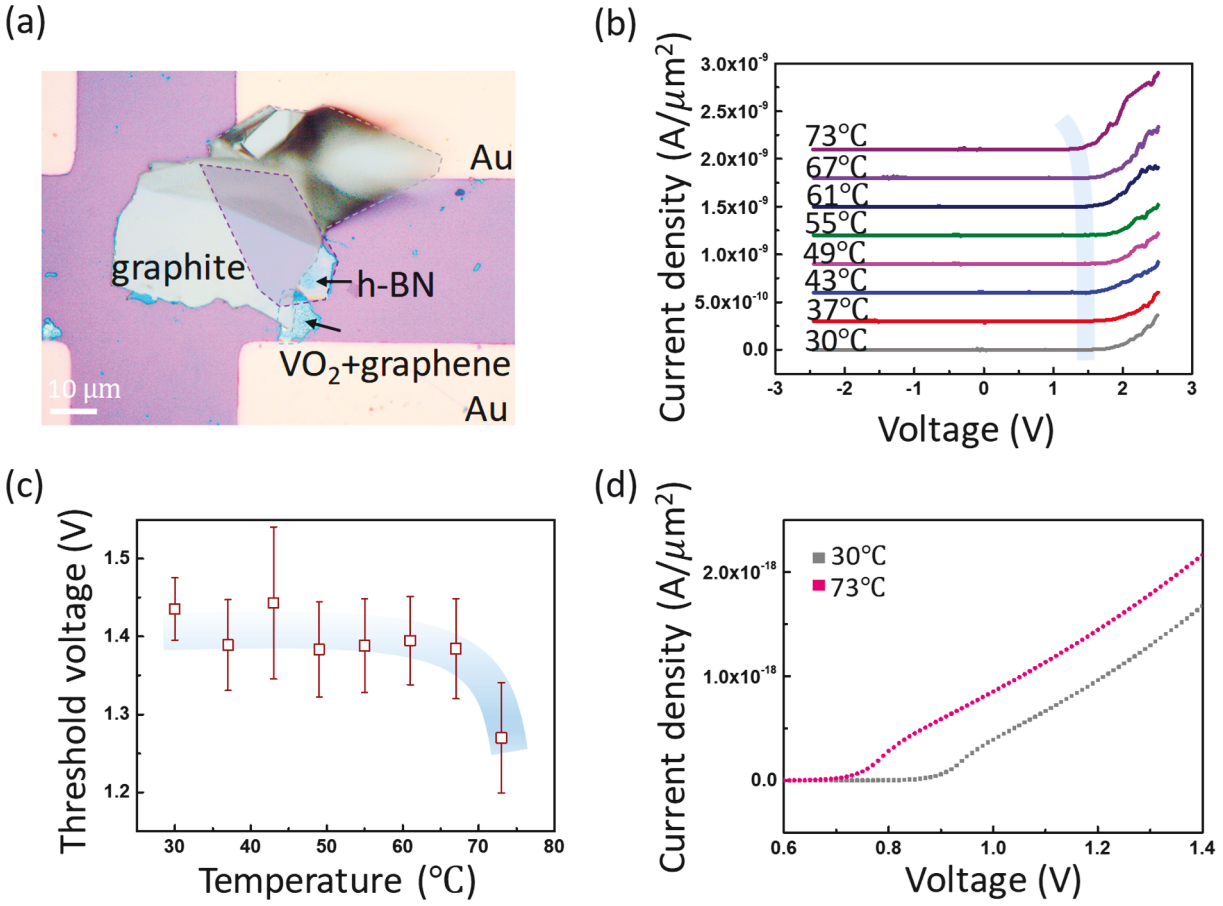

Figure 5. Reconfigurable remotely epitaxial VO_2 electrical heterostructure. (a) Optical image of the phase-change vertical diode device. (b) Current density vs voltage of the diode measured from 30 to 73 °C. (c) Threshold voltage of experimental $I-V$ curves in panel b at various temperatures. (d) Simulated $I-V$ curves (zoomed in at the threshold voltage region) at 30 and 73 °C for the h-BN thickness of 50 nm, barrier height between graphite and h-BN at 2 eV, and VO_2 work function difference remains at $\varphi_{HT}-\varphi_{RT}$ = 0.15 eV.

SiO_2 substrate via thermal release tape (see supplementary methods for details). We indeed see a lower intensity for VO_2 film at the metallic phase, the same as the intensity change across MIT temperature for single-crystal VO_2 nanobeams, as shown in Figure 4c. However, we are not able to see individual domains and how each domain switches phase as temperature changes. This may be attributed to the fact that the domain size is too small to be observed under an optical microscope. Further annealing or increasing the film deposition temperature may enlarge the domain size of VO_2, facilitating the in situ characterization of domain revolution across MIT temperature.

The temperature-dependent transmittance spectrum was also collected from VO_2 film on c-plane sapphire with a graphene layer from 3800 to 7800 cm^{-1} (Figure 4d,e). A hysteresis loop for transmittance signal collected at 4000 cm^{-1} (~0.50 eV) from 25 to 115 °C is obtained similarly to the optical intensity observed under a microscope.

Reconfigurable Transport Characteristics. Free-standing VO_2 film is obtained by peeling off VO_2 grown on graphene from c-plane sapphire using thermal release tape. After release, the film is transferred onto the SiO_2 substrate prepatterned with Au electrode pads (see supplementary methods and Figure S6 for details). It is found that VO_2 film always comes off together with graphene from the c-plane sapphire substrate, as confirmed by Raman spectroscopy (Figure S4). After transfer, cracks appear in VO_2-graphene films. However, for the local area, less than 20 μm, there is an absence of cracks (Figure S7). The success in obtaining free-standing VO_2 film provides a great opportunity to achieve many device structures for their specific applications, such as flexible sensors,[15] multistate memory devices,[51] and electrode for energy storage devices.[52]

Following the design in Figure 1a, we fabricate a vertical diode in the form of the phase-change heterostructure. Due to its processability and inertness, h-BN is an ideal insulating barrier between VO_2 and graphite.[53,54] Dry-transferred graphite is used as the top electrode. VO_2 film is utilized as a switchable layer sandwiched between the h-BN and bottom graphene electrode. Figure 5a shows an optical image of the device. The h-BN layer thickness is about 50 nm characterized by an atomic force microscope, as shown in Figure S8 (see supplementary methods for details).

As displayed in Figure 5b, diode current density has been measured at several different temperatures from 30 to 73 °C. Clearly, we see a very strong rectification featured by a few orders in the magnitude of the on/off ratio (rectification shows up when VO_2 is negatively biased). The on/off ratio is 3.7 × 10^2 at 30 °C and 1.7 × 10^3 at 73 °C at 2.4 V. In addition, we observe a shift of the threshold voltage for the onset of the rectification toward lower value along with increasing temperature (Figure 5c, Figure S9). The change in threshold voltage across temperature is closely related to the VO_2 work function change, which is about 0.15 eV across phase transition. This

DOI: 10.1021/acs.nanolett.9b02696
Nano Lett. XXXX, XXX, XXX−XXX

value agrees well with both experimental and simulated data. More discussion on this threshold voltage is in supplementary note 2.

To understand the rectifications, two major current-conducting mechanisms are discussed here: tunneling, and thermionic emission[55] as they represent two common mechanisms observed in insulators.[56] We simulate the tunneling current density based on (including image potential)[57]

$$J_{\text{tunnel}} = J_0\{\bar{\varphi}e^{-A_{\text{tun}}\bar{\varphi}^{1/2}} - (\bar{\varphi} + eV)e^{-A_{\text{tun}}(\bar{\varphi}+eV)^{1/2}}\} \quad (1)$$

where $J_0 = \frac{2}{2\pi h\Delta s^2}$, $A_{\text{tun}} = (2m)^{1/2}\left(\frac{4\pi\Delta s}{h}\right)$, Δs is the effective tunneling distance, $\bar{\varphi}$ is mean barrier height above the Fermi level of the negatively biased electrode, h is Planck's constant, e is electron charge, and V is the applied voltage. For tunneling, the forward bias is defined as the electrode with a lower work function (in our case, the VO_2 side) that is positively biased.

Forward bias:[57]

$$\bar{\varphi}_F = \varphi_2 - [(s_1 + s_2)/2s](eV + \Delta\varphi) - (1.15\lambda s/\Delta s)\ln[s_2(s - s_1)/s_1(s - s_2)] \quad (2)$$

Reverse bias:[57]

$$\bar{\varphi}_R = \varphi_1 + [(s_1 + s_2)/2s](\Delta\varphi - eV) - (1.15\lambda s/\Delta s)\ln[s_2(s - s_1)/s_1(s - s_2)] \quad (3)$$

where φ_1 and φ_2 are barrier heights in h-BN/VO_2 and h-BN/graphite interface, respectively. s_1 and s_2 are the limits of the barrier at Fermi level[57] with their difference as Δs. s is the thickness of the BN layer. $\Delta\varphi$ is the barrier height difference. λ is a constant inversely proportional to the thickness of the BN film and its dielectric constant. It can be seen that it is the difference between φ_1 and φ_2 that brings the asymmetric $I-V$ curves.

The thermionic current density considering image potential is simulated by[58]

$$J_{\text{thermionic}} = A_{\text{th}}T^2e^{-\varphi'_1/kT}(1 - e^{-eV/kT}) \quad (4)$$

where $A_{\text{th}} = \frac{4\pi mek^2}{h^3}$where φ'_1 is the maximum barrier heights above the Fermi level of the negatively biased electrode, T is temperature, m is effective carrier mass, k is Boltzmann constant, h is Planck's constant, e is electron charge, and V is the applied voltage.

Let J_1 and J_2 represent net current when the electrode of lower work function is negatively biased, namely, forward biased and positively biased, namely, reverse biased, respectively. We can plug φ'_1 into eq 4 to get thermionic current J_1 and J_2.

For $0 \le V \le \Delta\psi/e$, see the following:[58]

$$\varphi'_1 = \varphi_2 - eV - \frac{\{14.4[7 + \varepsilon_{ri}s(\Delta\varphi - eV)\}^{1/2}}{\varepsilon_{ri}s} \quad (5)$$

For $V \ge \Delta\psi/e$, see the following:[58]

$$\varphi'_1 = \varphi_1 - \frac{\{14.4[7 + \varepsilon_{ri}s(eV - \Delta\varphi)\}^{1/2}}{\varepsilon_{ri}s} \quad (6)$$

For all V when the diode is reverse biased, see the following:[58]

$$\varphi'_1 = \varphi_2 - \frac{\{14.4[7 + \varepsilon_{ri}s(\Delta\varphi + eV)\}^{1/2}}{\varepsilon_{ri}s} \quad (7)$$

Again, it is the difference between φ_1 and φ_2 that brings the asymmetric transport characteristics.

The total simulated current density is then

$$J_{\text{total}} = J_{\text{tunnel}} + J_{\text{thermionic}} \quad (8)$$

During electrical measurements, the positive electrode is connected to the side closer to h-BN (top electrode). Thus, the positive bias direction is the forward direction for thermionic current and the reverse direction for tunneling current. The dielectric constant of h-BN is 4.[53] The work function of graphite is approximately 5.5 eV,[59,60] and wide range values of work function for VO_2 in both the insulator phase and metal phase have been reported.[13,31,61] However, in an insulator−metal transition system, as a first-order approximation, the work function of the phase-change material is expected to become smaller at its insulator phase, especially when the insulator phase has n-type conductivity.[62] It is reported that VO_2, in general, behaves like n-type conductivity.[63−66] Thus, in our calculation, the work function of VO_2 is set as a variable. The charge carriers between the graphite electrode and VO_2 are set as electrons in the simulation. The effective mass of the carrier is taken as half of the electron mass, $0.5m_e$.[67]

Figure 5d shows an example of our simulated results with following assumptions: (1) the insulating phase of VO_2 is heavily doped so the conduction band minimum and the Fermi level is very close[68,69] (this is a reasonable assumption since the resistivity of the insulating phase is only a few orders in magnitude higher than that of the metal phase); (2) the voltage drop is mostly on h-BN (see Supplementary note 3); (3) the barrier height between h-BN and graphite is set as 2 eV. The barrier height between VO_2 and h-BN is calculated as the barrier height between h-BN and top graphite minus the work function difference between graphite and VO_2. The metallic phase VO_2 has a work function of 4.7 eV, and the insulating phase VO_2 possesses a work function of 4.55 eV with a work function decrease of 0.15 eV across MIT according to ref 61. The simulated current is dominated by the thermionic current, as expected, since h-BN is thick[56] (more discussion is shown in Figure S10). As we can see, the threshold voltage is related to the difference between the barrier height of VO_2 and h-BN and that of graphite and h-BN, thus, the work function difference between graphite and VO_2. When VO_2 is at the insulating phase (30 °C), the diode has a larger onset voltage and larger current density at 2.5 V (but lower current density at lower voltage) compared with the $I-V$ curve measured at 73 °C at the metallic VO_2 phase.

To further show the versatility of the device characterizes under optimized design condition, we simulate $I-V$ curves assuming various barrier height between h-BN and graphite with electrons as charge carriers (Figure S10a), different thicknesses of the insulating h-BN layer (Figure S10b), as well as difference magnitude of change in work function across MIT of VO_2 (Figure S10c) under both room temperature (30 °C) and high temperature (73 °C) (see supplementary note 4 for details). In our simulation, a single domain structure of the film

DOI: 10.1021/acs.nanolett.9b02696
Nano Lett. XXXX, XXX, XXX−XXX

is assumed, and at 73 °C, the whole film is approximated at its metal phase.

Both the experimental and the simulated results demonstrate that the vertical diode device based on band structure tuning induced by the phase transition of a switchable layer can significantly change the diode characteristics, such as current density and on/off ratio. This spectral weight engineering is not limited to VO_2. As long as this switchable layer of material has a controlled variation in the electronic structure under external stimuli (e.g., voltage-controlled in$NdNiO_3$, strain-induced MIT in $Sm_{0.5}Ca_{0.5}TiO_3$,[70] and electrochemical doping-induced MIT in $SmNiO_3$[71]), it can function as a switch to tune the diode behavior. This switchable layer can be optimized by maximizing its spectral weight change close to the Fermi level across phase transition to maximize the modification in diode characteristics.

CONCLUSION

We have successfully employed PLD to obtain free-standing VO_2 films by applying graphene as an interface layer between the c-plane sapphire substrate and VO_2 film. Better crystallinity and sharper $R-T$ transition of the VO_2 film grown on c-plane sapphire with a graphene layer than the film grown on bare c-plane sapphire substrate have been confirmed by XRD and electrical measurements, respectively. This high-quality VO_2 film is obtained due to a reduction in epitaxial strain, revealed by HRTEM and Cs-corrected STEM, from the partial screening of the strong VO_2-sapphire interaction. A vertical diode has been developed as a phase-change heterostructure, and it exhibits significant rectification (two to three orders in magnitude). The characteristics (such as threshold voltage and rectification ratio) of the diode can also be tuned by the VO_2 metal−insulator transition. Our work demonstrates a method to prepare high-quality crystalline free-standing thin films and promises their application to various novel device structures. It paves the way for the development of next-generation information processing and memory storage systems.

ASSOCIATED CONTENT

Supporting Information

The Supporting Information is available free of charge at https://pubs.acs.org/doi/10.1021/acs.nanolett.9b02696.

Methods, materials structure analysis, device characteristic analysis, the morphology of films, X-ray diffraction spectra of films, Raman spectra of films, device fabrication procedure, and device simulation results (PDF)

AUTHOR INFORMATION

Corresponding Authors

*Email: chenxc1213@mail.tsinghua.edu.cn (X.C.)
*Email: gaolei@ustb.edu.cn (L.G.)
*Email: shij4@rpi.edu (J.S.)

ORCID

Xin Sun: 0000-0001-5633-3371
Baiwei Wang: 0000-0002-4118-8826
Xinchun Chen: 0000-0001-7027-6799
Lei Gao: 0000-0001-8555-5168
Zonghuan Lu: 0000-0003-2375-8247
Jian Shi: 0000-0003-2115-2225

Author Contributions

○Y.G. and X.S.contributed equally to this work.

Author Contributions

J.S. conceived the project. Y.G. carried out the PLD growth and annealing of the VO_2 film, and peeled off free-standing VO_2 on graphene. X.S. provided graphene on c-plane sapphire and carried out Raman spectroscopy on transferred graphene. J.J. R.J. and Y.H. contributed on PLD growth. S.P. and Z.C. provided support in annealing the film. Y.G. collected the Raman spectrum and conducted resistance and optical contrast vs temperature measurements on VO_2. B.W. and Y.G. performed XRD characterization on VO_2 film. L.Z. carried out AFM characterization. Y.G. fabricated the vertical diode device and conducted the following electrical measurements on the device. X.C., X.Y.,W.Q. and L.G. conducted the microscopy experiments. Y.G. wrote the paper. All authors discussed the results and commented on the manuscript.

Notes

The authors declare no competing financial interest.

ACKNOWLEDGMENTS

We acknowledge the financial support on microscopy study from the National Key Research and Development Program of China (Grant No. 2017YFB0702100), National Natural Science Foundation of China (Grant No. 51727901, 51705017, 51975314, and U1706221). This material is based upon work supported by the Air Force Office of Scientific Research under award number FA9550-18-1-0116. The structural measurements are also supported by the NYSTAR Focus Center under award number C130117 and the NSF under award number CMMI 1635520. We also thank RPI Cleanroom and nanofabrication facility for device fabrication.

REFERENCES

(1) Ahn, C. H.; Triscone, J. M.; Mannhart, J. *Nature* **2003**, *424* (28), 1015−1018.
(2) Cavalleri, A.; Toth, C.; Siders, C. W.; Squier, J. A.; Raksi, F.; Forget, P.; Kieffer, J. C. *Phys. Rev. Lett.* **2001**, *87* (23), 237401.
(3) Newns, D.M.; Doderer, T.; Tsuei, C.C.; Donath, W.M.; Misewich, J.A.; Gupta, A.; Grossman, B.M.; Schrott, A.; Scott, B.A.; Pattnaik, P.C.; Gutfeld, R.J. v.; Sun, J.Z. *J. Electroceram.* **2000**, *4*, 339−344.
(4) Petrov, G. I.; Yakovlev, V. V.; Squier, J. A. *Opt. Lett.* **2002**, *27* (8), 655−657.
(5) Hormoz, S.; Ramanathan, S. *Solid-State Electron.* **2010**, *54* (6), 654−659.
(6) Katzke, H.; Tolédano, P.; Depmeier, W. *Phys. Rev. B: Condens. Matter Mater. Phys.* **2003**, *68* (2), 024109.
(7) Kim, H.-T.; Chae, B.-G.; Youn, D.-H.; Maeng, S.-L.; Kim, G.; Kang, K.-Y.; Lim, Y.-S. *New J. Phys.* **2004**, *6*, 52.
(8) Ruzmetov, D.; Gopalakrishnan, G.; Ko, C.; Narayanamurti, V.; Ramanathan, S. *J. Appl. Phys.* **2010**, *107* (11), 114516.
(9) Ruzmetov, D.; Senanayake, S. D.; Narayanamurti, V.; Ramanathan, S. *Phys. Rev. B: Condens. Matter Mater. Phys.* **2008**, *77* (19), 195442.
(10) Ruzmetov, D.; Zawilski, K. T.; Narayanamurti, V.; Ramanathan, S. *J. Appl. Phys.* **2007**, *102* (11), 113715.
(11) Yang, Z.; Ko, C.; Ramanathan, S. *Annu. Rev. Mater. Res.* **2011**, *41* (1), 337−367.
(12) Zhou, C.; Newns, D. M.; Misewich, J. A.; Pattnaik, P. C. *Appl. Phys. Lett.* **1997**, *70* (5), 598−600.
(13) Zhou, Y.; Ramanathan, S. *J. Appl. Phys.* **2013**, *113* (21), 213703.

DOI: 10.1021/acs.nanolett.9b02696
Nano Lett. XXXX, XXX, XXX−XXX

(14) Genchi, S.; Yamamoto, M.; Shigematsu, K.; Aritomi, S.; Nouchi, R.; Kanki, T.; Watanabe, K.; Taniguchi, T.; Murakami, Y.; Tanaka, H. *Sci. Rep.* **2019**, *9* (1), 2857.
(15) Li, X.; Yin, Z.; Zhang, X.; Wang, Y.; Wang, D.; Gao, M.; Meng, J.; Wu, J.; You, J. *Adv. Mater. Tech* **2019**, *4* (7), 1800695.
(16) Liu, D.; Cho, S. J.; Seo, J.-H.; Kim, K.; Kim, M.; Shi, J.; Yin, X.; Choi, W.; Zhang, C.; Kim, J.; Baboli, M. A.; Park, J.; Bong, J.; Lee, I.-K.; Gong, J.; Mikael, S.; Ryu, J. H.; Mohseni, P. K.; Li, X.; Gong, S.; Wang, X.; Ma, Z. *arXiv*, 2018.
(17) Kalikka, J.; Zhou, X.; Behera, J.; Nannicini, G.; Simpson, R. E. *Nanoscale* **2016**, *8* (42), 18212−18220.
(18) Chen, M.; Zhou, B.; Wang, F.; Xu, L.; Jiang, K.; Shang, L.; Hu, Z.; Chu, J. *RSC Adv.* **2018**, *8* (39), 21968−21974.
(19) Liu, Z.; Fei, Z.; Xu, C.; Jiang, Y.; Ma, X. L.; Cheng, H. M.; Ren, W. *Nanoscale* **2017**, *9* (22), 7501−7507.
(20) Yang, Y.; Hong, B.; Huang, H.; Luo, Z.; Gao, C.; Kang, C.; Li, X. *J. Mater. Sci.: Mater. Electron.* **2018**, *29* (3), 2561−2567.
(21) Dai, S.; Zhang, J.; Ma, Q.; Kittiwatanakul, S.; McLeod, A.; Chen, X.; Corder, S. G.; Watanabe, K.; Taniguchi, T.; Lu, J.; Dai, Q.; Jarillo-Herrero, P.; Liu, M.; Basov, D. N. *Adv. Mater.* **2019**, *31* (18), 1900251.
(22) Folland, T. G.; Fali, A.; White, S. T.; Matson, J. R.; Liu, S.; Aghamiri, N. A.; Edgar, J. H.; Haglund, R. F., Jr.; Abate, Y.; Caldwell, J. D. *Nat. Commun.* **2018**, *9* (1), 4371.
(23) Krishnamoorthy, H. N. S.; Zhou, Y.; Ramanathan, S.; Narimanov, E.; Menon, V. M. *Appl. Phys. Lett.* **2014**, *104*, 121101.
(24) Jiang, L.; Choi, W. S.; Jeen, H.; Dong, S.; Kim, Y.; Han, M. G.; Zhu, Y.; Kalinin, S. V.; Dagotto, E.; Egami, T.; Lee, H. N. *Nano Lett.* **2013**, *13* (12), 5837−5843.
(25) Falson, J. *Phys. E* **2019**, *110*, 49−51.
(26) Lotnyk, A.; Hilmi, I.; Ross, U.; Rauschenbach, B. *Nano Res.* **2018**, *11* (3), 1676−1686.
(27) Lu, Z.; Sun, X.; Xie, W.; Littlejohn, A.; Wang, G. C.; Zhang, S.; Washington, M. A.; Lu, T. M. *Nanotechnology* **2018**, *29* (44), 445702.
(28) Kim, Y.; Cruz, S. S.; Lee, K.; Alawode, B. O.; Choi, C.; Song, Y.; Johnson, J. M.; Heidelberger, C.; Kong, W.; Choi, S.; Qiao, K.; Almansouri, I.; Fitzgerald, E. A.; Kong, J.; Kolpak, A. M.; Hwang, J.; Kim, J. *Nature* **2017**, *544* (7650), 340−343.
(29) Jeong, J.; Min, K.-A.; Kang, B. K.; Shin, D. H.; Yoo, J.; Yang, W. S.; Lee, S. W.; Hong, S.; Hong, Y. J. *Appl. Phys. Lett.* **2018**, *113* (23), 233103.
(30) Jeong, J.; Min, K. A.; Shin, D. H.; Yang, W. S.; Yoo, J.; Lee, S. W.; Hong, S.; Hong, Y. J. *Nanoscale* **2018**, *10* (48), 22970−22980.
(31) Sohn, A.; Kim, H.; Kim, D.-W.; Ko, C.; Ramanathan, S.; Park, J.; Seo, G.; Kim, B.-J.; Shin, J.-H.; Kim, H.-T. *Appl. Phys. Lett.* **2012**, *101* (19), 191605.
(32) Li, J.; Dho, J. *J. Cryst. Growth* **2010**, *312* (22), 3287−3291.
(33) Guo, Y. X.; Liu, Y. F.; Zou, C. W.; Qi, Z. M.; Wang, Y. Y.; Xu, Y. Q.; Wang, X. L.; Zhang, F.; Zhou, R. *Appl. Phys. A: Mater. Sci. Process.* **2014**, *115* (4), 1245−1250.
(34) Kodu, M.; Berholts, A.; Kahro, T.; Kook, M.; Ritslaid, P.; Seemen, H.; Avarmaa, T.; Alles, H.; Jaaniso, R. *Beilstein J. Nanotechnol.* **2017**, *8*, 571−578.
(35) Kodu, M.; Berholts, A.; Kahro, T.; Avarmaa, T.; Kasikov, A.; Niilisk, A.; Alles, H.; Jaaniso, R. *Appl. Phys. Lett.* **2016**, *109* (11), 113108.
(36) Nan, H. Y.; Ni, Z. H.; Wang, J.; Zafar, Z.; Shi, Z. X.; Wang, Y. Y. *J. Raman Spectrosc.* **2013**, *44* (7), 1018−1021.
(37) Moatti, A.; Sachan, R.; Prater, J.; Narayan, J. *ACS Appl. Mater. Interfaces* **2017**, *9* (28), 24298−24307.
(38) Yang, M.; Yang, Y.; Hong, B.; Wang, L.; Luo, Z.; Li, X.; Kang, C.; Li, M.; Zong, H.; Gao, C. *RSC Adv.* **2015**, *5* (98), 80122−80128.
(39) Yang, T.-H.; Mal, S.; Jin, C.; Narayan, R. J.; Narayan, J. *Appl. Phys. Lett.* **2011**, *98* (2), 022105.
(40) Chen, C.; Zhu, Y.; Zhao, Y.; Lee, J. H.; Wang, H.; Bernussi, A.; Holtz, M.; Fan, Z. *Appl. Phys. Lett.* **2010**, *97* (21), 211905.
(41) Porter, D.A.; Easterling, K.E.; Sherif, M. Y. *Phase transformations in metals and alloys*, 3rd ed.; CRC Press, 2016.
(42) Ghosh, P.; Kumar, S.; Ramalingam, G.; Kochat, V.; Radhakrishnan, M.; Dhar, S.; Suwas, S.; Ghosh, A.; Ravishankar, N.; Raghavan, S. *J. Phys. Chem. C* **2015**, *119* (5), 2513−2522.
(43) Paik, H.; Moyer, J. A.; Spila, T.; Tashman, J. W.; Mundy, J. A.; Freeman, E.; Shukla, N.; Lapano, J. M.; Engel-Herbert, R.; Zander, W.; Schubert, J.; Muller, D. A.; Datta, S.; Schiffer, P.; Schlom, D. G. *Appl. Phys. Lett.* **2015**, *107* (16), 163101.
(44) Brassard, D.; Fourmaux, S.; Jean-Jacques, M.; Kieffer, J. C.; El Khakani, M. A. *Appl. Phys. Lett.* **2005**, *87* (5), 051910.
(45) Jeong, J.; Aetukuri, N.; Graf, T.; Schladt, T. D.; Samant, M. G.; Parkin, S. S. P. *Science* **2013**, *339* (6126), 1402.
(46) Nakano, M.; Shibuya, K.; Okuyama, D.; Hatano, T.; Ono, S.; Kawasaki, M.; Iwasa, Y.; Tokura, Y. *Nature* **2012**, *487* (7408), 459−462.
(47) Cao, J.; Ertekin, E.; Srinivasan, V.; Fan, W.; Huang, S.; Zheng, H.; Yim, J. W.; Khanal, D. R.; Ogletree, D. F.; Grossman, J. C.; Wu, J. *Nat. Nanotechnol.* **2009**, *4* (11), 732−737.
(48) Wang, Y.; Seewald, L.; Sun, Y. Y.; Keblinski, P.; Sun, X.; Zhang, S.; Lu, T. M.; Johnson, J. M.; Hwang, J.; Shi, J. *Adv. Mater.* **2016**, *28* (40), 8975.
(49) Wu, J.; Gu, Q.; Guiton, B. S.; de Leon, N. P.; Ouyang, L.; Park, H. *Nano Lett.* **2006**, *6* (10), 2313−2317.
(50) Laverock, J.; Jovic, V.; Zakharov, A. A.; Niu, Y. R.; Kittiwatanakul, S.; Westhenry, B.; Lu, J. W.; Wolf, S. A.; Smith, K. E. *Phys. Rev. Lett.* **2018**, *121* (25), 256403.
(51) Pellegrino, L.; Manca, N.; Kanki, T.; Tanaka, H.; Biasotti, M.; Bellingeri, E.; Siri, A. S.; Marre, D. *Adv. Mater.* **2012**, *24* (21), 2929−2934.
(52) Nethravathi, C.; Rajamathi, C. R.; Rajamathi, M.; Gautam, U. K.; Wang, X.; Golberg, D.; Bando, Y. *ACS Appl. Mater. Interfaces* **2013**, *5* (7), 2708−2714.
(53) Barrera, S. C. Theory of graphene−insulator−graphene tunnel junctions. In *Layered Two-Dimensional Heterostructures and Their Tunneling Characteristics*; Springer, 2017; p 87.
(54) Wang, L.; Meric, I.; Huang, P. Y.; Gao, Q.; Gao, Y.; Tran, H.; Taniguchi, T.; Watanabe, K.; Campos, L. M.; Muller, D. A.; Guo, J.; Kim, P.; Hone, J.; Shepard, K. L.; Dean, C. R. *Science* **2013**, *342*, 614−617.
(55) Chin, M. L.; Periasamy, P.; O'Regan, T. P.; Amani, M.; Tan, C.; O'Hayre, R. P.; Berry, J. J.; Osgood, R. M., III; Parilla, P. A.; Ginley, D. S.; Dubey, M. *J. Vac. Sci. Technol., B: Nanotechnol. Microelectron.: Mater., Process., Meas., Phenom.* **2013**, *31* (5), 051204.
(56) Sze, S. M.; Ng, K. K. *Physics of Semiconductor Devices*, 3rd ed.; John Wiley & Sons, Inc., 2007.
(57) Simmons, J. G. *J. Appl. Phys.* **1963**, *34* (9), 2581−2590.
(58) Simmons, J. G. *J. Appl. Phys.* **1964**, *35* (8), 2472−2481.
(59) Sygellou, L.; Paterakis, G.; Galiotis, C.; Tasis, D. *J. Phys. Chem. C* **2016**, *120* (1), 281−290.
(60) Misra, A.; Kalita, H.; Kottantharayil, A. *ACS Appl. Mater. Interfaces* **2014**, *6* (2), 786−794.
(61) Ko, C.; Yang, Z.; Ramanathan, S. *ACS Appl. Mater. Interfaces* **2011**, *3* (9), 3396−3401.
(62) Imada, M.; Fujimori, A.; Tokura, Y. *Rev. Mod. Phys.* **1998**, *70* (4), 1039.
(63) Simo, A.; Mwakikunga, B.; Sone, B. T.; Julies, B.; Madjoe, R.; Maaza, M. *Int. J. Hydrogen Energy* **2014**, *39* (15), 8147−8157.
(64) Wu, J. M.; Liou, L. B. *J. Mater. Chem.* **2011**, *21* (14), 5499.
(65) Maeng, J.; Kim, T.-W.; Jo, G.; Lee, T. *Mater. Res. Bull.* **2008**, *43* (7), 1649−1656.
(66) Ruzmetov, D.; Heiman, D.; Claflin, B. B.; Narayanamurti, V.; Ramanathan, S. *Phys. Rev. B: Condens. Matter Mater. Phys.* **2009**, *79* (15), 153107.
(67) Britnell, L.; Gorbachev, R. V.; Jalil, R.; Belle, B. D.; Schedin, F.; Mishchenko, A.; Georgiou, T.; Katsnelson, M. I.; Eaves, L.; Morozov, S. V.; Peres, N. M. R.; Leist, J.; Geim, A. K.; Novoselov, K. S.; Ponomarenko, L. A. *Science* **2012**, *335* (24), 947−950.
(68) Powell, R. J.; Berglund, C. N.; Spicer, W. E. *Phys. Rev.* **1969**, *178* (3), 1410−1415.
(69) Eyert, V. *Ann. Phys.* **2002**, *11* (9), 650−702.

DOI: 10.1021/acs.nanolett.9b02696
Nano Lett. XXXX, XXX, XXX−XXX

(70) Yoshimatsu, K.; Okabe, H.; Oshima, T.; Ueda, S.; Ohtomo, A. *Phys. Rev. B: Condens. Matter Mater. Phys.* **2016**, *93* (19), 195159.
(71) Shi, J.; Zhou, Y.; Ramanathan, S. *Nat. Commun.* **2014**, *5*, 4860.

DOI: 10.1021/acs.nanolett.9b02696
Nano Lett. XXXX, XXX, XXX−XXX